

1 **Estimating the impact of a major hurricane on**
2 **transport processes**

3 Thomas Dobbelaere, Emmanuel Hanert

4 March 4, 2021

5 **Abstract**

6 In most hydrodynamic model studies, currents and waves are simu-
7 lated separately. This is especially true for the simulation of passive
8 drifters, whose trajectories are often computed based solely on cur-
9 rents. Although this simplification holds for most situations, as the force
10 exerted by waves on currents can be neglected in fair weather condi-
11 tions, it may lead to significant errors during storm conditions, when
12 currents are strongly influenced by wind-generated waves. In this study,
13 we investigate current-wave interactions in heavy-wind conditions by
14 coupling the unstructured-mesh hydrodynamic model SLIM with the
15 wave model SWAN. We apply the coupled model in the Florida Reef
16 Tract during Hurricane Irma (Sep. 2017) and show that it successfully
17 reproduces both the observed wave behavior and storm surge during
18 the hurricane. The modeled currents were then used to simulate the
19 trajectories of passive drifters during the passage of the hurricane. Our
20 results show that taking wave force into account induces variations of
21 up 1 m/s in modelled currents on the continental shelf break as well
22 as in the vicinity of reefs and islands. Wave-current interactions can
23 therefore deflect the trajectories of drifting material by up to 10 km on
24 the passage of the storm **Add something?**. These results strongly advo-
25 cate for the inclusion of wave forces while studying transport processes
26 (sediments, pollutants, larvae, etc.) in heavy-wind conditions.

²⁷ **1 Introduction**

²⁸ Wave-current interactions in coastal areas are of great importance for coastal
²⁹ engineering as they play a key role in sediment transport, morphological
³⁰ evolution and pollutant mixing (Bever and MacWilliams, 2013; Li and Johns,
³¹ 1998). However, these interactions are highly nonlinear and can vary sig-
³² nificantly in space and time (Wu et al., 2011). Wave-induced currents are
³³ generated by wave radiation gradients (Longuet-Higgins, 1970), affecting
³⁴ water levels near shorelines and wave breaking points (Longuet-Higgins
³⁵ and Stewart, 1964), while changes in water levels and currents, in turn,
³⁶ affect the motion and evolution of the waves (Sikirić et al., 2013). Cou-
³⁷ pled wave-current models are therefore required to capture these complex
³⁸ interactions.

³⁹ As coastal oceans are characterized by complex topology with islands,
⁴⁰ inlets and estuaries, unstructured (usually two-dimensional) models are pre-
⁴¹ ferred as structured grid models show limitations in resolving topologically-
⁴² controlled nearshore processes (Wu et al., 2011; Chen et al., 2007). The
⁴³ effect of wave-interactions becomes even more significant in the case of
⁴⁴ hurricanes, that generate large wind-waves and disturb ocean conditions
⁴⁵ (Liu et al., 2020) by causing coastal upwellings on continental shelves
⁴⁶ (Smith, 1982) and inducing strong currents, waves and storm surges in
⁴⁷ nearshore and coastal regions (Dietrich et al., 2010; Weisberg and Zheng,
⁴⁸ 2006). South Florida and the Gulf of Mexico are particularly vulnerable to
⁴⁹ hurricanes (Malmstadt et al., 2009) and modelling studies predict tropical
⁵⁰ cyclones to increase both in frequency and intensity in this region (Mar-
⁵¹ sooli et al., 2019; Knutson et al., 2010). Being able to accurately model
⁵² wave-current interactions in this area becomes thus critical.

⁵³ Individual-based modelling of particulates has been extensively used to
⁵⁴ study the transport of drifting materials such as pollutants, sediments or
⁵⁵ larvae (Garcia-Pineda et al., 2020; Liubartseva et al., 2018; Figueiredo et al.,
⁵⁶ 2013; Frys et al., 2020). Although some of these studies take the impact
⁵⁷ of waves into account by adding a Stokes drift velocity, *i.e.* the net drift of a
⁵⁸ floating particle in the direction of the wave propagation (Van Den Bremer
⁵⁹ and Breivik, 2018), to the Eulerian currents, they usually neglect the wave-
⁶⁰ induced currents. Such practice is reasonable in the case of fair weather,

61 when wave-induced forces exerted on currents are relatively smaller, but
62 might lead to significant inaccuracies during storm conditions. To assess
63 the importance of wave-current interactions during a tropical cyclone, we
64 investigated the transport of drifting particulates on the Florida shelf during
65 Hurricane Irma, one of the strongest and costliest tropical cyclones on
66 records in the Atlantic Basin (Chen et al., 2007), that made landfall in Florida
67 in September 2017.

68 In this study, we developed an unstructured coupled wave-current model of
69 South Florida to simulate the ocean circulation during hurricane Irma. Both
70 modelled currents and waves were validated against field measurements
71 and were then used to simulate the transport of drifting material in the
72 Florida Keys and the Florida inner shelf during the storm. Model outputs
73 were then compared with uncoupled simulation results in order to assess
74 the impact of wave-induced forces and Stokes drift on the modelled currents
75 and transports.

76 **2 Methods**

77 **2.1 Study area and observational data**

78 Large-scale ocean circulation around South Florida is dominated by the
79 Florida Current (FC), which originates from the Loop Currents (LC) where it
80 enters the Florida Straits from the Gulf of Mexico, and, downstream, forms
81 the Gulf Stream. The FC is a major western boundary current character-
82 ized by spatial variability and meandering, associated with the presence
83 of cyclonic eddies between the core of the current and the complex reef
84 topography of the Florida Reef Tract (FRT) (Lee et al., 1995; Kourafalou and
85 Kang, 2012). The northern half of these reefs are made of early Holocene
86 reef frameworks and indurated sand ridges while the southern part (the
87 Florida Keys) is composed of a chain of limestone islands, fossilized rem-
88 nants of ancient coral reefs and sand bars (Hoffmeister and Multer, 1968;
89 Shinn, 1988; Lidz and Shinn, 1991). The variability of the FC extends over
90 a large range of spatial and temporal scales, with periods of 30-70 days in
91 the Lower Keys (Lee et al., 1995) and shorter periods of 2-21 days in the
92 Upper Keys (Lee and Mayer, 1977), and exhibits significant seasonal and

93 interannual cycles (Johns and Schott, 1987; Lee and Williams, 1988; Schott
94 et al., 1988). Circulation on the West Florida Shelf (WFS) on the other hand
95 is forced by local winds and tidal fluctuations (Lee and Smith, 2002; Liu and
96 Weisberg, 2012).

97 The state of the ocean around Florida is monitored by an extensive array
98 of tide gauges, current meters and buoys. In this study, we used sea
99 surface elevation measurements from the National Oceanic and Atmospheric
100 Administrations (NOAA) Tides and Currents dataset. These measurements
101 were taken at four locations: two in the Florida Keys (Key West and Vaca
102 Key); one on the eastern coast of Florida (Key West); and one on the western
103 coast (Naples). For the currents, we used ADCP measurements from
104 the University of South Florida's College of Marine Science's (USF/CMS)
105 Coastal Ocean Monitoring and Prediction System (COMPS) for the WFS
106 (Weisberg et al., 2009). More specifically, we used measurements from
107 moorings C10, C12 and C13, respectively located at the 25, 50, and 50
108 m isobaths of the WFS (Liu et al., 2020). Finally, for the waves, we used
109 measurements from four buoys of the NOAA's National Data Buoy Center
110 (NDBC). Two on Florida's Eastern shelf and two on the WFS. The locations
111 of all measurement stations are shown on Fig. 1

112 **2.2 Wind and atmospheric pressure during Hurricane Irma**

113 Irma made landfall in Florida on 10 September 2017 as a category 3 storm,
114 first at Cudjoe Key (Florida Keys) and later on Marco Island, south to Naples
115 (see hurricane track in Fig. 1). It then weakened to a category 2 storm as it
116 moved further inland (Pinelli et al., 2018). The storm caused damages to
117 up to 75% of the buildings at his landfall point in the Florida Keys, making it
118 one of the strongest and costliest hurricanes on record in the Atlantic basin
119 (Xian et al., 2018; Zhang et al., 2019). The strongest reported wind speed
120 was 50 m/s on Marco Island while the highest recorded storm surge was
121 2.3 m, although larger wind speed likely occurred in the Florida Keys (Pinelli
122 et al., 2018) In order to reproduce the wind profile of Irma in our model,
123 we used high-resolution H*Wind wind fields (Powell et al., 1998). As these
124 data represent 1-min averaged wind speeds, we multiplied them by a factor
125 0.93 to obtain 10-min averaged wind speeds (Harper et al., 2010), which

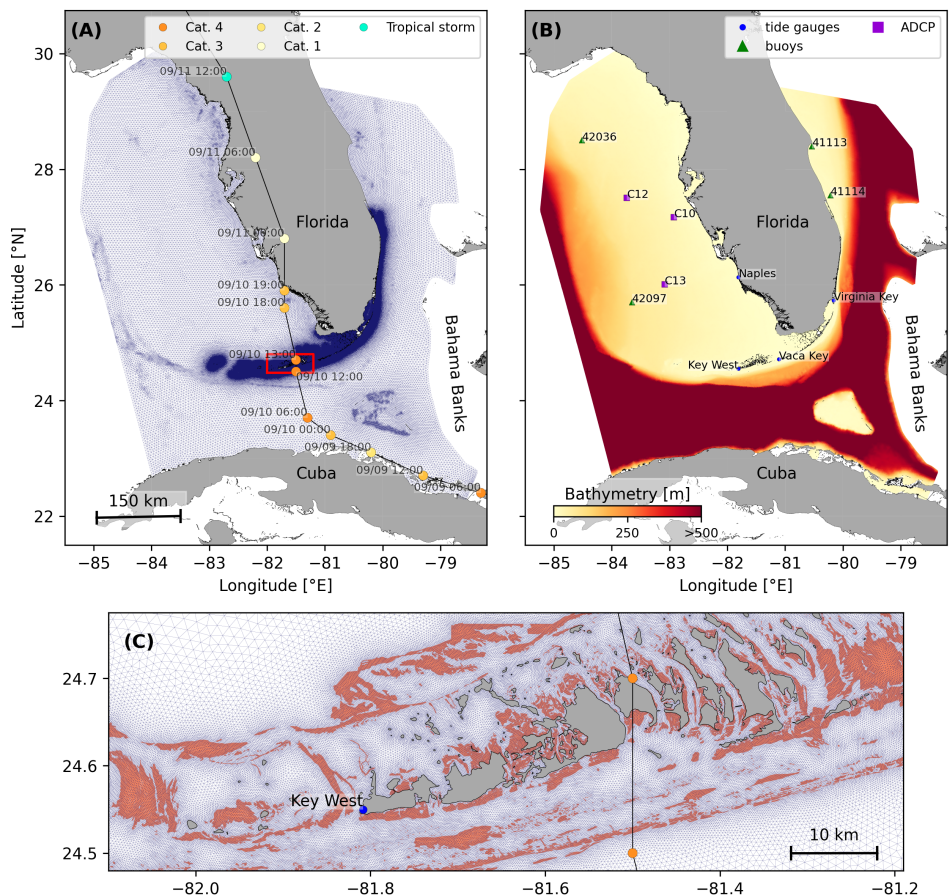


Fig. 1: **A:** Mesh of the computational domain with the trajectory of Irma, category of the hurricane is given by the Saffir-Simpson color scale. **B:** Bathymetry of the domain with the location of stations used for the validation of the model outputs. **C:** Close up view of the Lower Keys area, where the mesh resolution reaches 100m near reefs (shown in coral) and islands (highlighted in dark grey)

126 are more consistent with the time step of our model. Furthermore, H*Wind
 127 wind profiles did not cover the whole model extent during the hurricane and
 128 were thus blended within coarser wind field extracted from ECMWF ERA-5
 129 datasets. Pressure fields of Irma were also constructed using ERA-5 data.
 130 However, the coarse resolution of the data set caused the depression at the
 131 center of the hurricane to get smoothed out, leading to an underestimation of
 132 the pressure gradient in our model. To better capture the central depression
 133 of Irma, we built a hybrid pressure field using the position and the minimal
 134 pressure of the core of the hurricane based on its track as recorded in
 135 the HURDAT 2 database (Landsea and Franklin, 2013). Based on this
 136 information, the hybrid pressure field was constructed by combining an
 137 idealized Holland pressure profile (Lin and Chavas, 2012) within the radius
 138 of maximum wind speed of Irma (Knaff et al., 2018) with ERA-5 pressure
 139 field. The transition between from the Holland profile to ERA-5 data outside
 140 the radius of maximum wind speed data was performed using a smooth step
 141 function.

142 **2.3 Hydrodynamic model**

143 Ocean currents generated during hurricane Irma around South Florida were
 144 modelled using the 2D barotropic version of the unstructured-mesh coastal
 145 ocean model SLIM¹. The model mesh covers an area similar to the model
 146 extent of Dobbelaere et al. (2020b), that includes the FRT but also the Florida
 147 Strait and part of the Gulf of Mexico (Figure 1). However, this area has
 148 been slightly extended northeastward and westward in order to include the
 149 NOAA-NDBC buoys. Furthermore, in order to withstand potential cell drying
 150 during the hurricane, we solved the conservative shallow water equations
 151 with wetting-drying:

$$\begin{aligned}
 \frac{\partial H}{\partial t} + \nabla \cdot (\mathbf{U}) &= 0 , \\
 \frac{\partial \mathbf{U}}{\partial t} + \nabla \cdot \left(\frac{\mathbf{U}\mathbf{U}}{H} \right) &= - f \mathbf{e}_z \times \mathbf{U} + \alpha g H \nabla(H - h) - \frac{1}{\rho} \nabla p_{\text{atm}} + \frac{1}{\rho} \boldsymbol{\tau}_s \quad (1) \\
 &\quad + \nabla \cdot (\nu \nabla \mathbf{U}) - \frac{C_b}{H^2} |\mathbf{U}| \mathbf{U} + \gamma (\mathbf{U}_* - \mathbf{U}) ,
 \end{aligned}$$

¹<https://www.slim-ocean.be>

152 where H is the water column height and \mathbf{U} is the depth-averaged transport;
 153 f is the Coriolis coefficient; g is the gravitational acceleration; h is the
 154 bathymetry; α is a coefficient stating whether the mesh element is wet
 155 ($\alpha = 1$) or dry ($\alpha = 0$); ν is the viscosity; C_b is the bulk bottom drag
 156 coefficient; ∇p_{atm} is the atmospheric pressure gradient; τ_s is the surface
 157 stress due to wind; and γ is a relaxation coefficient towards a reference
 158 transport \mathbf{U}_* . As in Frys et al. (2020) and Dobbelaere et al. (2020b), SLIM
 159 currents were gradually relaxed towards HYCOM (Chassignet et al., 2007) in
 160 regions where the water depth exceeds 50m.

161 At very high wind speeds, the white cap is blown off the crest of the waves,
 162 which generates a layer of droplets that acts as a slip layer for the winds
 163 at the ocean-atmosphere interface (Holthuijsen et al., 2012). This causes
 164 a saturation of the wind drag coefficient for strong winds (Donelan et al.,
 165 2004; Powell et al., 2003). To account for the impact of this saturation
 166 on the surface wind stress in our model, we implemented the wind drag
 167 parameterization of Moon et al. (2007). In this parameterization, the drag
 168 coefficient C_d depends on the wind speed at 10-m height U_{10} according to:

$$C_d = \kappa^2 \log \left(\frac{10}{z_0} \right)^{-2} \quad (2)$$

169 where κ is the von Karman constant. The roughness length z_0 in Eq. (2) is
 170 expressed as:

$$z_0 = \begin{cases} \frac{0.0185}{g} U_*^2 & \text{if } U_{10} \leq 12.5 \text{ m/s ,} \\ [0.085(-0.56U_*^2 + 20.255U_* + 2.458) - 0.58] \times 10^{-3} & \text{if } U_{10} > 12.5 \text{ m/s ,} \end{cases} \quad (3)$$

171 with U_* the friction velocity. The relation between U_{10} and U_* is given by:

$$U_{10} = -0.56U_*^2 + 20.255U_* + 2.458 . \quad (4)$$

172 The mesh resolution depends on the distance to coastlines and reefs follow-
 173 ing the approach of (Dobbelaere et al., 2020b). The mesh was then further
 174 refined as a function of bathymetry and bathymetry gradient, as suggested
 175 by SWAN documentation². Such approach improves the efficiency of the

²<http://swanmodel.sourceforge.net/unswan/unswan.htm>

176 computational grid by locally increasing the mesh resolution in areas where
 177 the bathymetry or evolution of the waves change rapidly while avoiding to
 178 invest too many computational resources where the physics or depth change
 179 less. The mesh was generated using the Python library seamsh³, based
 180 on the the open-source mesh generator GMSH (Geuzaine and Remacle,
 181 2009). It is composed of approximately 7.7×10^5 elements. The coarsest
 182 elements, far away from the FRT, had a characteristic length size of about 5
 183 km whereas the finest elements had a characteristic length of 100 m near
 184 coastlines and reefs (Fig 1).

185 **2.4 Wave model**

186 Waves were modelled using the parallel unstructured-mesh version of the
 187 Simulating WAves Nearshore (SWAN) model (Booij et al., 1999), one of the
 188 most commonly used wave models in coastal areas and inland waters. This
 189 model solves the action balance equation, which reads (Mei, 1989):

$$\frac{\partial N}{\partial t} + \nabla_{\mathbf{x}} \cdot [(\mathbf{c}_g + \mathbf{u})N] + \frac{\partial}{\partial \theta}[c_\theta N] + \frac{\partial}{\partial \sigma}[c_\sigma N] = \frac{S_{in} + S_{ds} + S_{nl}}{\sigma}, \quad (5)$$

190 where $N = E/\sigma$ is the wave action density; θ is the wave propagation
 191 direction; σ is the wave relative frequency; c_g is the wave group velocity,
 192 $\mathbf{u} = \mathbf{U}/H$ is SLIM depth-averaged current velocity; c_θ and c_σ are the propa-
 193 gation velocities in spectral space due to refraction and shifting in frequency
 194 due to variations in depth and currents; and S_{in} , S_{ds} , and S_{nl} respectively
 195 represent wave growth by wind, wave decay and nonlinear transfers of
 196 wave energy through interactions between triplets and quadruplets. Spectra
 197 were discretized with 48 direction bins and 50 frequency bins logarithmically
 198 distributed from 0.3 to 2 Hz. Exponential wind growth was parameterized
 199 using the formulation of Janssen (1991), while dissipations by whitecapping
 200 and bottom dissipations followed the formulations of Komen et al. (1984)
 201 and Madsen et al. (1989) respectively. Coefficients for exponential wind
 202 growth and whitecapping parameterizations were based on the results of
 203 Siadatmousavi et al. (2011), and significantly differ from SWAN's default
 204 settings. By default, SWAN implements the wind input formulation of Komen
 205 et al. (1984) and the steepness-dependent coefficient governing dissipation

³<https://pypi.org/project/seamsh/>

206 by whitecapping is a linear function of the wave number. In this study, this
 207 steepness-dependent coefficient is a quadratic function of the wave number,
 208 as it showed better predictions of the significant wave height in the study of
 209 Siadatmousavi et al. (2011). The choice of these formulations was motivated
 210 by the appearance of numerical instabilities in the region of the Gulf Stream
 211 using SWAN's default parameter values. Finally, wave boundary conditions
 212 were derived from WAVEWATCH III (Tolman et al., 2009) spectral outputs at
 213 buoy locations. Surface wave induce a net drift in te direction of the wave
 214 propagation, known as Stokes drift (Van Den Bremer and Breivik, 2018;
 215 Stokes, 1880). This net drift has significant impacts on sediment motion
 216 in near shore regions (Hoefel and Elgar, 2003), the formation of Langmuir
 217 cells (Langmuir, 1938; Craik and Leibovich, 1976) as well as the transport of
 218 heat, salt or pollutants such as oil or micro-plastic in the upper ocean layer
 219 (McWilliams and Sullivan, 2000; Röhrs et al., 2012; Drivedal et al., 2014).
 220 To model adequately the Stokes profile in mixed wind-driven sea and swell
 221 conditions, the full two- dimensional wave spectrum must be represented
 222 by a spectral wave model within a wave-current coupling (Van Den Bremer
 223 and Breivik, 2018). In this study, depth-averaged Stokes drift was therefore
 224 computed by SWAN using the following formula:

$$\mathbf{u}_s = \int_0^{2\pi} \int_0^{+\infty} \frac{\sigma^3}{h \tanh(2kh)} E(\sigma, \theta) (\cos \theta, \sin \theta) d\sigma d\theta , \quad (6)$$

225 where k is the norm of the wave vector; h is the water depth; and $E(\sigma, \theta)$ is
 226 the wave energy density.

227 2.5 Coupled model

228 SLIM and SWAN are coupled so that they run on the same computational
 229 core and the same unstructured mesh. SLIM is run first and passes com-
 230 puted wind velocities (\mathbf{U}_{10}), water levels ($\eta = H - h$) and depth-averaged
 231 currents ($\mathbf{u} = \mathbf{U}/H$) to SWAN, as well as a roughness length (z_0) for the bot-
 232 tom dissipation formulation of Madsen et al. (1989). This roughness length
 233 is computed from SLIM's bulk drag coefficient C_b following the approach of
 234 Dietrich et al. (2011) so that both models have consistent bottom dissipation
 235 parameterizations. SWAN then utilizes these quantities to compute the wave
 236 radiation stress gradient, that is then passed to SLIM as the wave-induced

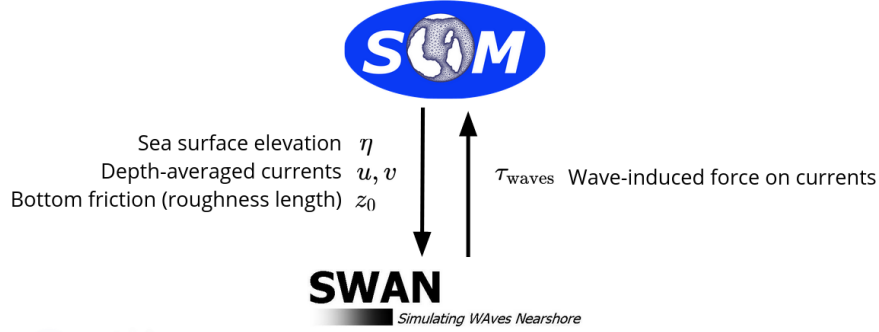


Fig. 2: Schematic illustration of the coupled SLIM+SWAN model.

stress on currents τ_{wave} . SLIM then uses this quantity to update the value of the surface stress τ_s in Eq. (1), that now becomes the sum of wind and wave-induced stresses $\tau_s = \tau_{\text{wind}} + \tau_{\text{wave}}$.

SLIM equations are integrated using an implicit scheme while SWAN is unconditionally stable (Dietrich et al., 2010), allowing both models to be run with relatively large time steps. In this study, both models were therefore run sequentially using a time step of 600s, so that each computational core was alternating running either SLIM or SWAN. As in the coupling between SWAN and ADCIRC (Dietrich et al., 2010), both models utilize the same local sub-mesh, allowing for a one-to-one correspondence between the geographic locations of the mesh vertices. No interpolation is therefore needed when passing computed quantities from a model to another, which allows for efficient inter-model communication. However, as SLIM applies discontinuous Galerkin finite element methods, an additional conversion step to a continuous framework was required to transmit SLIM nodal quantities to SWAN.

3 Results

We first validated the reconstructed atmospheric fields of hurricane Irma as well the modelled currents and waves of our coupled model against fields measurements. Once we had built some confidence in our model accuracy, these modelled quantities were used to model transport of passive drifters in the Lower Keys on the passage of the hurricane. These drifters

259 were advected by two sets of currents: (i) the currents from an uncoupled
260 SLIM simulation of Irma (SLIM) and (ii) the currents modelled by the cou-
261 pled SLIM+SWAN model (SLIM+SWAN). Furthermore, the depth-averaged
262 Stokes drift was computed using our coupled model (Stokes_C) and an
263 uncoupled SWAN simulation of the hurricane (Stokes_U). We then simulated
264 the trajectories of passive drifters on the passage of the Irma in the Lower
265 Keys using different combinations of these fields. These trajectories were
266 finally compared to evaluate the impact of the wave-current interactions and
267 the Stokes drift on the transport processes during a major hurricane.

268 **3.1 Model validation**

269 H*Wind winds and hybrid pressure field agree well with station measure-
270 ments at Vaca Key station (Fig. 3). The hybrid pressure field shows better
271 agreement with observations than ERA-5 pressure as it successfully re-
272 produces the storm depression. ERA-5 fields, on the other hand, fail to
273 resolve the low pressure at the core of the hurricane due to their coarser
274 grid, leading to an overestimation of 8 mbar of the storm depression. Both
275 H*Wind and ERA-5 agree well with observed wind speeds although both
276 data sets tend to slightly overestimate the width and intensity of the wind
277 peak. However, H*wind profiles show a better match with the timing of the
278 observed peak, as ERA-5 winds tend to anticipate it. H*wind also exhibits a
279 slightly narrower peak in wind speed, which better agrees with observations.
280 Hydrodynamic outputs of the coupled wave-current agree well with tide
281 gauge (Fig. 4) and ADCP measurements (Fig. 5). The timing and amplitude
282 of the storm surges are well reproduced by the coupled model, the largest
283 model error being an overestimation of 18 cm of the elevation peak at
284 Virginia Key. The fit is especially good at Naples, where both the positive
285 and negative surges are captured by the coupled model with an error of less
286 than 5 cm. This result is of interest as negative surges, although less studied,
287 affect water exchanges between the estuaries and the coastal ocean and
288 disturb the benthic ecosystems (Liu et al., 2020). Modelled 2D currents were
289 validated against depth-averaged ADCP measurements at mooring station
290 C10, C12 and C13 (Fig. 5). As in Liu et al. (2020), the vector correlation
291 analysis of Kundu (1976) is performed to compare modelled and observed

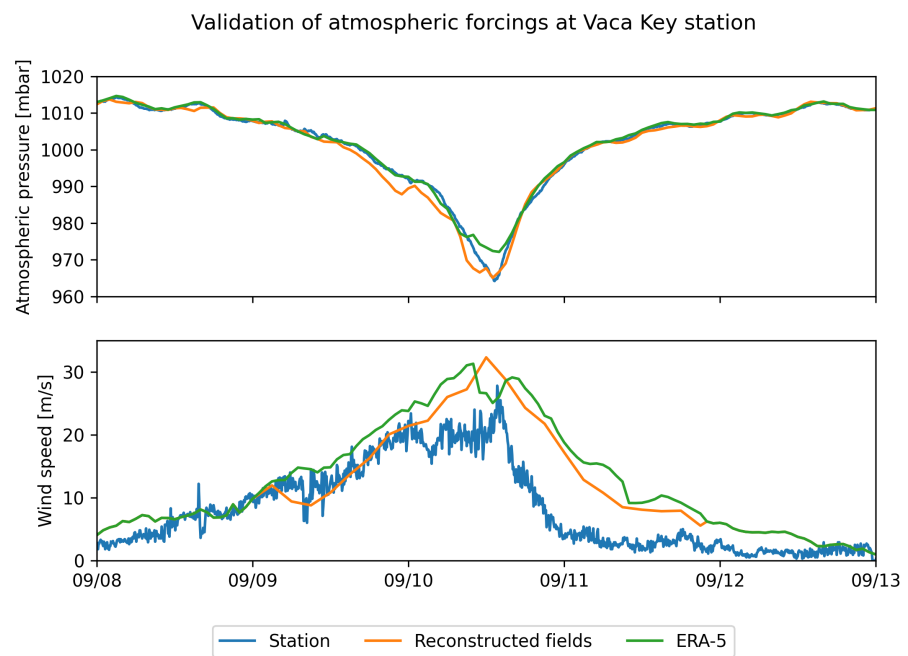


Fig. 3: Comparison of reconstructed wind atmospheric pressure with field measurements and coarser ECMWF ERA-5 profiles at Vaca Key station. The generated hybrid atmospheric forcings better capture the observed storm depression while H*wind winds better match the measured peak in wind speed.

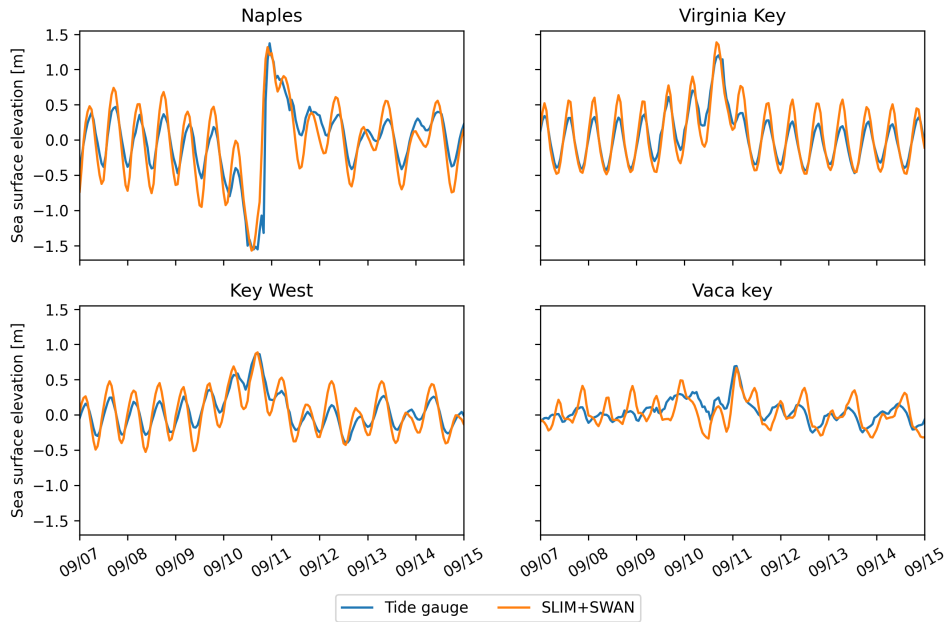


Fig. 4: Comparison of modelled sea surface elevation with all 4 tide gauge measurements (see Fig. 1B for their location). Timing and amplitudes of the storm surges are well reproduced by the model

292 current velocity vectors. Correlation coefficients (ρ) between simulated
 293 and observed depth-averaged currents were 0.84, 0.74 and 0.73 at the
 294 C10, C12 and C13 locations, respectively. Average veering angles were
 295 computed as well and were below 12° , as in (Liu et al., 2020). However, in
 296 our case, no clear tendency regarding modelled current behavior compared
 297 to observations was observed. As expected from a depth-averaged model,
 298 the best fit with observations is obtained at the shallowest mooring C10,
 299 located on the 25m isobath, with an average veering angle of 6° .
 300 The simulated significant wave height agrees well with observations on the
 301 WFS, where errors on the peak value do not exceed 5%. On the East Florida
 302 Shelf, errors are slightly larger reaching 20%. Although the model outputs
 303 agree well with observations, a lag in significant wave height is observed
 304 for all 4 buoys. Moreover, the peak in significant wave height tends to be
 305 underestimated at buoys 41113 and 41114, located on the East Florida Shelf.
 306 Other wave parameters were better reproduced by the model on the WFS as
 307 well, as illustrated for buoy 42036 in Fig. 6. This good fit on the WFS is not
 308 surprising as the parameters used for wind energy input and whitecapping

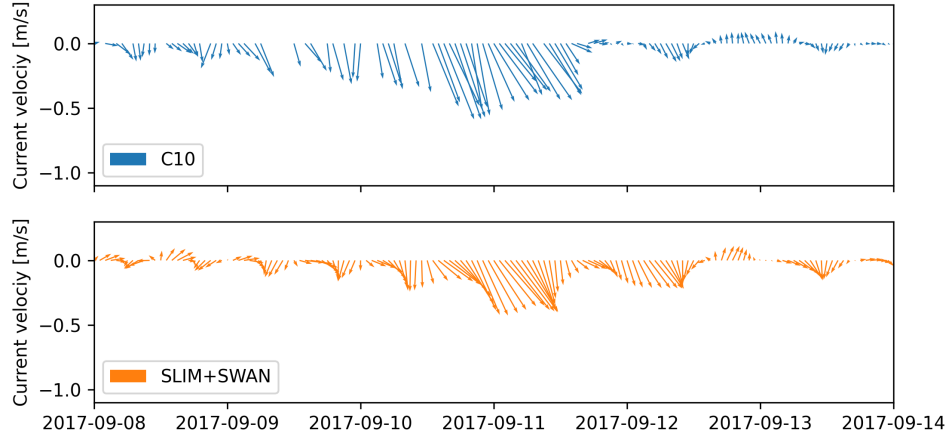


Fig. 5: Comparison of modelled current velocity with observed velocity at mooring C10 (see Fig. 1B for its location). Modelled current velocities agree well with observations, with a correlation coefficient of 0.83 and an average veering angle of 6° .

309 dissipation were based on the calibration performed by (Siadatmousavi et al.,
 310 2011) on the Northern Gulf of Mexico. Wind-induced wave growth might
 311 therefore be underestimated on the eastern shelf. Consequently, incident
 312 wave do not receive enough energy to grow after breaking on the bank
 313 boundary, leading to an underestimation of the significant wave height at
 314 the location of the buoys. Nonetheless, as this study focused on the wave
 315 produced by Irma, that made landfall on the western coasts of Florida, the
 316 use of parameterizations calibrated for the Gulf of Mexico seems reasonable.

317 3.2 Impact of waves on currents and transport

318 We evaluated the impact of wave-current interactions on modelled currents
 319 during the passage of Irma in the Lower Keys, between the 7 September
 320 and the 13 September 2017. First, we computed the maximum difference
 321 between currents modelled by SLIM and SLIM+SWAN during this period
 322 (Fig. 7A). The largest differences in currents were observed over reefs, on
 323 the shelf break and around islands and can reach 1 m/s, with SLIM+SWAN
 324 currents having the largest amplitude. These areas of strong current differ-
 325 ences correspond to the regions where the largest wave-induced stress
 326 τ_{wave} occurred (7B), as wave breaking and wave slowing down over rough

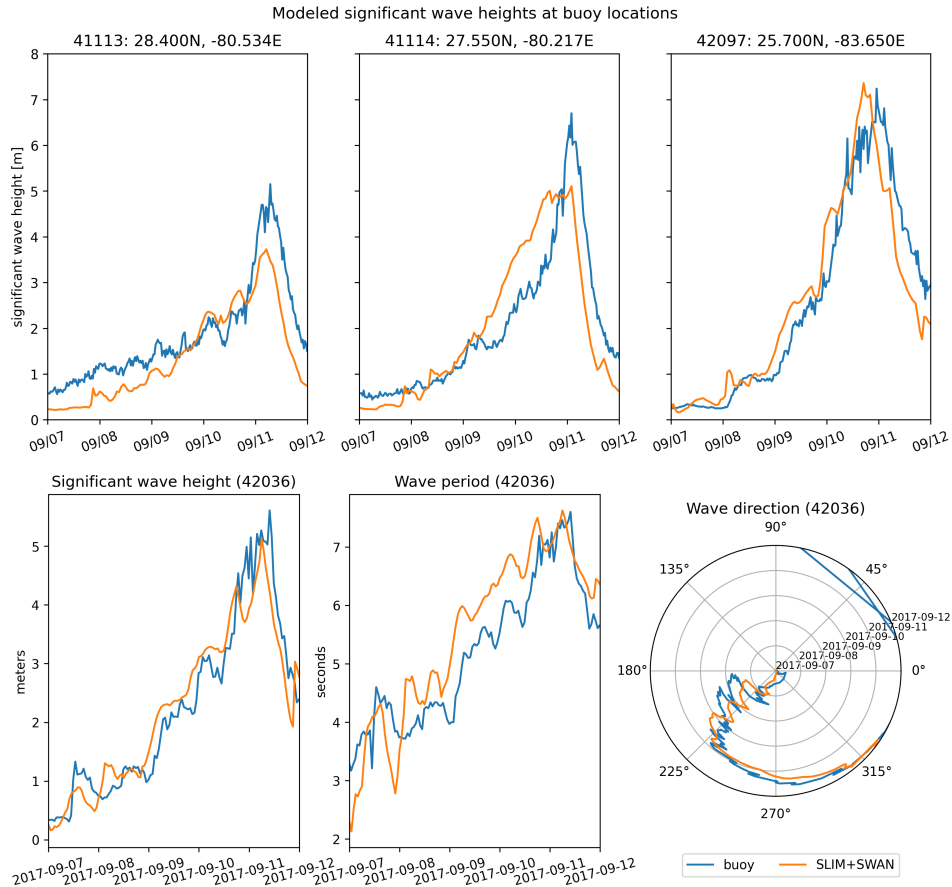


Fig. 6: Comparison of modelled wave parameters with observation at the 4 buoys location (locations shown in Fig. 1B). Modelled significant wave height agrees well with field measurement. As model parameters were calibrated for the Northern Gulf of Mexico, observations are better reproduced at buoys located on the WFS, as illustrated for buoy 42036

327 seabed induce variations of the wave radiation stress (Longuet-Higgins and
328 Stewart, 1964). Wave-induced differences in current velocity were amplified
329 by the action of the wind stress τ_{wind} (Fig. 7C). Wind speeds were larger in
330 the front right quadrant of the hurricane (Zedler et al., 2009), causing the
331 difference in current velocities to be larger on the right side of the storm
332 trajectory. This is especially clear in the area between the Florida Keys
333 and the Everglades, where relatively small values of the radiation stress
334 gradient produced strong differences in current velocity of up to 0.5 m/s in
335 combination with the action of the winds.

336 To quantify the impact of these differences in velocity fields, we compared the
337 trajectories of virtual particles advected by SLIM and SLIM+SWAN currents
338 during the passage of Irma in the Lower Keys (Fig. 8). These particles were
339 released on the inner and outer shelves in the areas highlighted by red and
340 blue dots in Fig. 8 on 7 September and were tracked until 15 September.
341 These areas were constructed using backtracking methods (Dobbelaeere
342 et al., 2020a) to ensure that the release particles would intersect the path
343 of Irma during its passage in the Florida Keys. We first defined two 25km^2
344 regions on the trajectory of the hurricane (see circles on Fig. 8). Particles
345 within these two regions were then tracked back in time using uncoupled
346 SLIM currents between the passage of the hurricane in the 7 of September,
347 defining the two release regions of Fig. 8. We then compared the trajectories
348 of particles originating from these regions and advected forward in time by
349 different sets of currents: (i) uncoupled SLIM currents alone; (ii) coupled
350 SLIM+SWAN currents; (iii) SLIM currents with the depth-averaged Stokes
351 drift computed by our coupled model (Stokes_C); (iv) SLIM+SWAN currents
352 with Stokes_C; and (v) SLIM currents with the depth-averaged Stokes drift
353 computed by uncoupled SWAN (Stokes_U). This comparison was performed
354 by computing the distances between the centers of mass of the simulated
355 clouds of particles through time.

- 356 • The impact of wave-current interactions is mostly important during the
357 passage of the hurricane but negligible on the rest of the simulated pe-
358 riod. This is best exemplified by the comparison of clouds of particles
359 advected by SLIM and SLIM+SWAN on the inner shelf. The distance
360 between the centers of mass of these clouds peaks at 5km during the
361 passage Irma but tends to zero during the rest of the simulated period

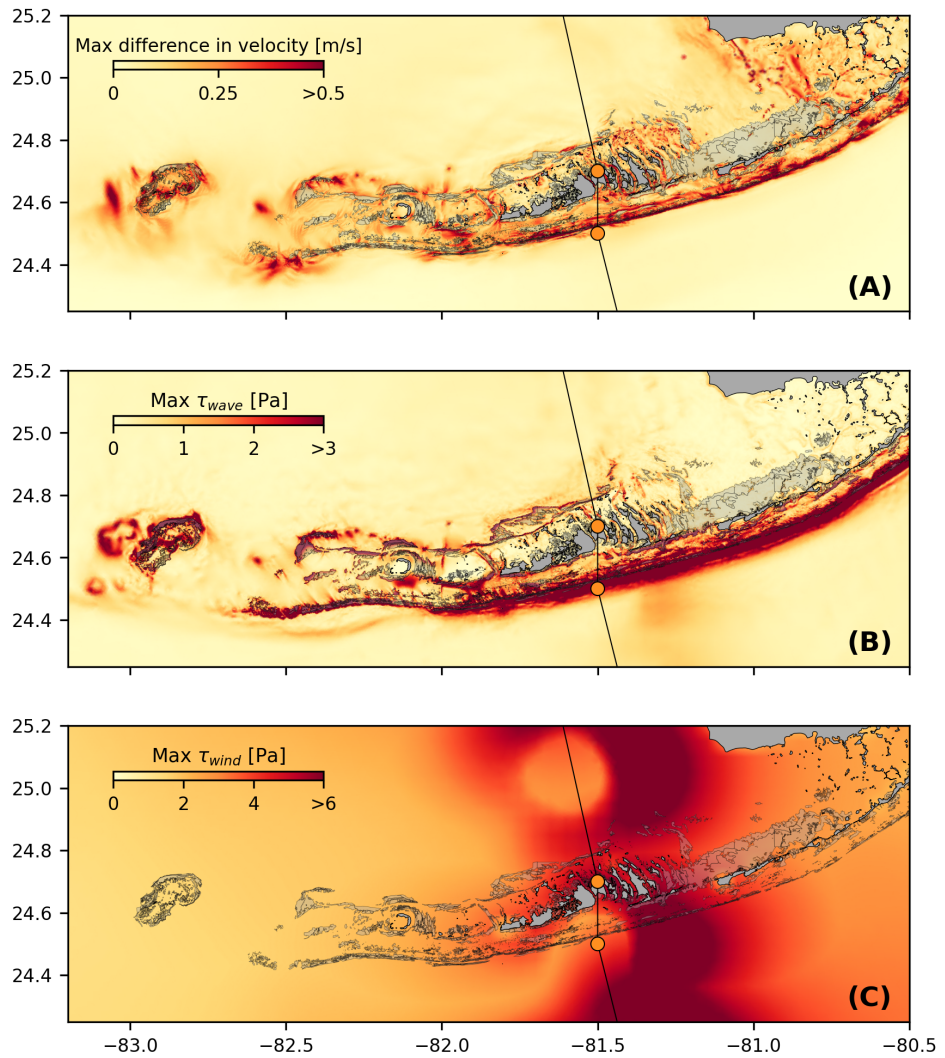


Fig. 7: Maximum difference between SLIM and SLIM+SWAN currents **(A)** during the passage of Irma in the Lower Florida Keys, along with the maximum wave radiation stress gradient τ_{wave} **(B)** and wind stress τ_{wind} **(C)** generated by the hurricane. Wave-induced stress yields difference larger than 0.5 m/s in current velocities. These wave-induced differences in currents were amplified by the action of the asymmetric wind profile of Irma, with larger differences occurring on the right of the storm trajectory

- 362 • The impact of the Stokes drift is larger than the impact of the wave-
 363 current interactions on the inner shelf (<5km for SLIM vs SLIM+SWAN
 364 and almost 10 km for SLIM vs SLIM+Stokes_C and SLIM+SWAN+Stokes_C).
 365 However, on the outer shelf, SLIM vs. SLIM+SWAN and SLIM vs
 366 SLIM+SWAN+Stokes_C show similar values. This difference between
 367 the inner and outer shelf can be explained by the sheltering on the
 368 inner shelf due to reefs and islands as well as wave breaking on the
 369 shelf break
- 370 • On the inner shelf, the distance between the centers of mass of the
 371 particle clouds stabilizes after the passage of the hurricane while this
 372 distance keeps increasing during to days after the passage of the
 373 hurricane on the outer shelf under the action of the Stokes drift. This
 374 shows the strong impact of wave-induced transport in the open ocean.
- 375 • Impact of Stokes drift and wave-current interactions weaker on the
 376 inner shelf. Max. distance of about 5 km between the centers of mass
 377 of the clouds of particles compared to 30km on the outer shelves
- 378 • The fact that SLIM+Stokes_C vs. SLIM+Stokes_U keeps increasing on
 379 the outer shelf after the passage of the hurricane shows the impact of
 380 the strong current velocities of the FC on the modelled Stokes drift
- 381 • Nonetheless, the differences between the two modelled Stokes drifts
 382 remains relatively small with a maximum value of 2km between the
 383 centers of mass of the simulated particle clouds. Furthermore, as
 384 SLIM vs SLIM+SWAN+Stokes and SLIM vs. SLIM+Stokes_C show
 385 similar values on the inner shelf, this suggests that the combination
 386 of currents and Stokes drifts produces sufficientl accurate results on
 387 sheltered shallow areas such as the WFS. However, neglecting the
 388 wave-current interactions leads to differences of up to 5km in modelled
 389 particle trajectories on the outer shelf.

390 4 Discussion and conclusions

391 Impact of waves on coral connectivity

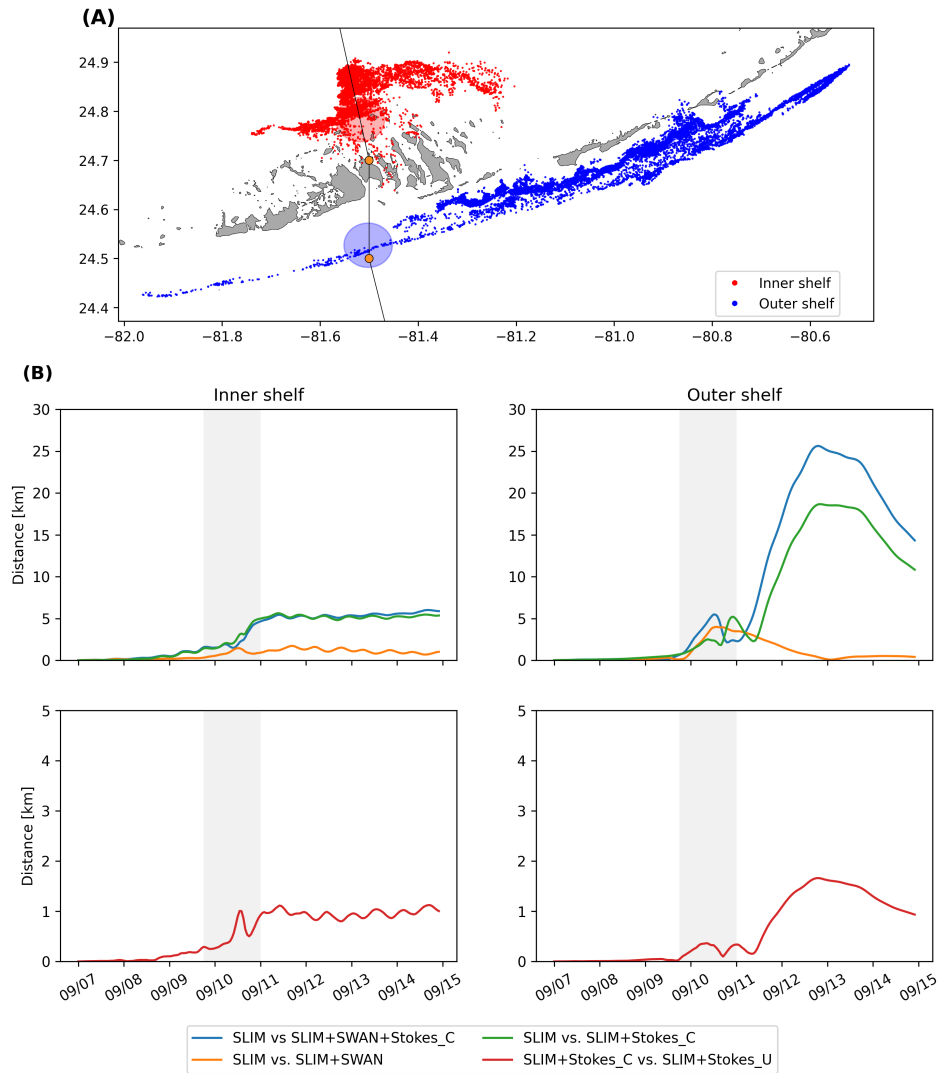


Fig. 8: **A:** Release regions of the passive drifters on the inner and outer shelves (dots) constructed from the 25km^2 (circles) areas on the trajectory of Irma. **B:** Comparison of the trajectories of drifters released from the regions highlighted in **A** and advected by different combinations of coupled and uncoupled velocity fields.

392 Ability of wave model to correctly capture gradient in significant wave height
393 due to current-waves interactions under tropical cyclones depends on:

- 394 • Broad perspective ⇒ not limited to FL
- 395 • Mention search and rescue
- 396 • However, ignoring waves in storm conditions could result in significant
397 inaccuracies in modelled trajectories, as illustrated in the case of
398 release region 2 in Fig. 8
- 399 • Spatial (10km → 5km) and spectral (36 dir. → 48 dir.) resolution
400 (Hegermiller et al., 2019)
- 401 • Directional spreading of incident waves (Villas Bôas et al., 2020)

402 **Conflict of Interest Statement**

403 The authors declare that the research was conducted in the absence of any
404 commercial or financial relationships that could be construed as a potential
405 conflict of interest.

406 **Author Contributions**

407 **Funding**

408 **Acknowledgments**

409 Computational resources were provided by the Consortium des Équipements
410 de Calcul Intensif (CÉCI), funded by the F.R.S.-FNRS under Grant No. 2.5020.11.
411 Thomas Dobbelaere is a PhD student supported by the Fund for Research
412 training in Industry and Agriculture (FRIA/FNRS).

413 **Supplementary Material**

414 The Supplementary Material for this article is attached to the submitted
415 document.

416 **References**

- 417 Bever, A. J. and MacWilliams, M. L. (2013). Simulating sediment transport
418 processes in San Pablo Bay using coupled hydrodynamic, wave, and
419 sediment transport models. *Marine Geology*, 345:235–253.
- 420 Booij, N., Ris, R. C., and Holthuijsen, L. H. (1999). A third-generation wave
421 model for coastal regions: 1. Model description and validation. *Journal*
422 *of geophysical research: Oceans*, 104(C4):7649–7666.
- 423 Chassignet, E. P., Hurlbert, H. E., Smedstad, O. M., Halliwell, G. R., Hogan,
424 P. J., Wallcraft, A. J., Baraille, R., and Bleck, R. (2007). The HYCOM
425 (hybrid coordinate ocean model) data assimilative system. *Journal of*
426 *Marine Systems*, 65(1-4):60–83.
- 427 Chen, C., Huang, H., Beardsley, R. C., Liu, H., Xu, Q., and Cowles, G. (2007).
428 A finite volume numerical approach for coastal ocean circulation studies:
429 Comparisons with finite difference models. *Journal of Geophysical*
430 *Research: Oceans*, 112(C3).
- 431 Craik, A. D. and Leibovich, S. (1976). A rational model for Langmuir circula-
432 tions. *Journal of Fluid Mechanics*, 73(3):401–426.
- 433 Dietrich, J., Bunya, S., Westerink, J., Ebersole, B., Smith, J., Atkinson,
434 J., Jensen, R., Resio, D., Luettich, R., Dawson, C., et al. (2010). A
435 high-resolution coupled riverine flow, tide, wind, wind wave, and storm
436 surge model for southern Louisiana and Mississippi. part ii: Synoptic
437 description and analysis of hurricanes Katrina and Rita. *Monthly Weather*
438 *Review*, 138(2):378–404.
- 439 Dietrich, J., Westerink, J., Kennedy, A., Smith, J., Jensen, R., Zijlema, M.,
440 Holthuijsen, L., Dawson, C., Luettich, R., Powell, M., et al. (2011).
441 Hurricane Gustav (2008) waves and storm surge: Hindcast, synoptic

- 442 analysis, and validation in southern Louisiana. *Monthly Weather Review*,
443 139(8):2488–2522.
- 444 Dobbelaere, T., Muller, E., Gramer, L., Holstein, D., and Hanert, E. (2020a).
445 Report on the potential origin of the SCTLD in the Florida Reef Tract.
446 Available online at: [https://floridadep.gov/rcp/coral/documents/
447 report-potential-origin-sctld-florida-reef-tract](https://floridadep.gov/rcp/coral/documents/report-potential-origin-sctld-florida-reef-tract).
- 448 Dobbelaere, T., Muller, E. M., Gramer, L. J., Holstein, D. M., and Hanert, E.
449 (2020b). Coupled epidemic-hydrodynamic modeling to understand the
450 spread of a deadly coral disease in Florida. *Frontiers in Marine Science*,
451 7:1016.
- 452 Donelan, M., Haus, B., Reul, N., Plant, W., Stiassnie, M., Gruber, H., Brown,
453 O., and Saltzman, E. (2004). On the limiting aerodynamic roughness of
454 the ocean in very strong winds. *Geophysical Research Letters*, 31(18).
- 455 Drivdal, M., Broström, G., and Christensen, K. (2014). Wave-induced mixing
456 and transport of buoyant particles: application to the statfjord a oil spill.
457 *Ocean Science*, 10(6):977–991.
- 458 Figueiredo, J., Baird, A. H., and Connolly, S. R. (2013). Synthesizing larval
459 competence dynamics and reef-scale retention reveals a high potential
460 for self-recruitment in corals. *Ecology*, 94(3):650–659.
- 461 Frys, C., Saint-Amand, A., Le Hénaff, M., Figueiredo, J., Kuba, A., Walker, B.,
462 Lambrechts, J., Vallaey, V., Vincent, D., and Hanert, E. (2020). Fine-
463 scale coral connectivity pathways in the Florida Reef Tract: implications
464 for conservation and restoration. *Frontiers in Marine Science*, 7:312.
- 465 Garcia-Pineda, O., Androulidakis, Y., Le Hénaff, M., Kourafalou, V., Hole,
466 L. R., Kang, H., Staples, G., Ramirez, E., and DiPinto, L. (2020). Mea-
467 suring oil residence time with GPS-drifters, satellites, and Unmanned
468 Aerial Systems (UAS). *Marine pollution bulletin*, 150:110644.
- 469 Geuzaine, C. and Remacle, J.-F. (2009). Gmsh: A 3-d finite element mesh
470 generator with built-in pre-and post-processing facilities. *International
471 journal for numerical methods in engineering*, 79(11):1309–1331.

- 472 Harper, B., Kepert, J., and Ginger, J. (2010). *Guidelines for converting*
473 *between various wind averaging periods in tropical cyclone conditions.*
474 Citeseer.
- 475 Hegermiller, C. A., Warner, J. C., Olabarrieta, M., and Sherwood, C. R.
476 (2019). Wave–current interaction between Hurricane Matthew wave
477 fields and the Gulf Stream. *Journal of Physical Oceanography*,
478 49(11):2883–2900.
- 479 Hoefel, F. and Elgar, S. (2003). Wave-induced sediment transport and
480 sandbar migration. *Science*, 299(5614):1885–1887.
- 481 Hoffmeister, J. and Multer, H. (1968). Geology and origin of the Florida Keys.
482 *Geological Society of America Bulletin*, 79(11):1487–1502.
- 483 Holthuijsen, L. H., Powell, M. D., and Pietrzak, J. D. (2012). Wind and waves
484 in extreme hurricanes. *Journal of Geophysical Research: Oceans*,
485 117(C9).
- 486 Janssen, P. A. (1991). Quasi-linear theory of wind-wave generation applied
487 to wave forecasting. *Journal of physical oceanography*, 21(11):1631–
488 1642.
- 489 Johns, W. E. and Schott, F. (1987). Meandering and transport variations
490 of the Florida Current. *Journal of physical oceanography*, 17(8):1128–
491 1147.
- 492 Knaff, J. A., Sampson, C. R., and Musgrave, K. D. (2018). Statistical tropi-
493 cal cyclone wind radii prediction using climatology and persistence:
494 Updates for the western North Pacific. *Weather and Forecasting*,
495 33(4):1093–1098.
- 496 Knutson, T. R., McBride, J. L., Chan, J., Emanuel, K., Holland, G., Landsea,
497 C., Held, I., Kossin, J. P., Srivastava, A., and Sugi, M. (2010). Tropical
498 cyclones and climate change. *Nature geoscience*, 3(3):157–163.
- 499 Komen, G., Hasselmann, S., and Hasselmann, K. (1984). On the exis-
500 tence of a fully developed wind-sea spectrum. *Journal of physical*
501 *oceanography*, 14(8):1271–1285.

- 502 Kourafalou, V. H. and Kang, H. (2012). Florida Current meandering and
503 evolution of cyclonic eddies along the Florida Keys Reef Tract: Are they
504 interconnected? *Journal of Geophysical Research: Oceans*, 117(C5).
- 505 Kundu, P. K. (1976). Ekman veering observed near the ocean bottom.
506 *Journal of Physical Oceanography*, 6(2):238–242.
- 507 Landsea, C. W. and Franklin, J. L. (2013). Atlantic hurricane database un-
508 certainty and presentation of a new database format. *Monthly Weather
509 Review*, 141(10):3576–3592.
- 510 Langmuir, I. (1938). Surface motion of water induced by wind. *Science*,
511 87(2250):119–123.
- 512 Lee, T. N., Leaman, K., Williams, E., Berger, T., and Atkinson, L. (1995).
513 Florida Current meanders and gyre formation in the southern Straits
514 of Florida. *Journal of Geophysical Research: Oceans*, 100(C5):8607–
515 8620.
- 516 Lee, T. N. and Mayer, D. A. (1977). Low-frequency current variability and
517 spin-off eddies along the shelf off southeast Florida. *Collected Reprints*,
518 1(1):344.
- 519 Lee, T. N. and Smith, N. (2002). Volume transport variability through the
520 Florida Keys tidal channels. *Continental Shelf Research*, 22(9):1361–
521 1377.
- 522 Lee, T. N. and Williams, E. (1988). Wind-forced transport fluctuations of the
523 Florida Current. *Journal of Physical Oceanography*, 18(7):937–946.
- 524 Li, Z. and Johns, B. (1998). A three-dimensional numerical model of surface
525 waves in the surf zone and longshore current generation over a plane
526 beach. *Estuarine, Coastal and Shelf Science*, 47(4):395–413.
- 527 Lidz, B. H. and Shinn, E. A. (1991). Paleoshorelines, reefs, and a rising sea:
528 South florida, usa. *Journal of Coastal Research*, pages 203–229.
- 529 Lin, N. and Chavas, D. (2012). On hurricane parametric wind and appli-
530 cations in storm surge modeling. *Journal of Geophysical Research:
531 Atmospheres*, 117(D9).

- 532 Liu, Y. and Weisberg, R. H. (2012). Seasonal variability on the West Florida
533 shelf. *Progress in Oceanography*, 104:80–98.
- 534 Liu, Y., Weisberg, R. H., and Zheng, L. (2020). Impacts of hurricane Irma
535 on the circulation and transport in Florida Bay and the Charlotte Harbor
536 estuary. *Estuaries and Coasts*, 43(5):1194–1216.
- 537 Liubartseva, S., Coppini, G., Lecci, R., and Clementi, E. (2018). Tracking
538 plastics in the Mediterranean: 2D Lagrangian model. *Marine pollution
539 bulletin*, 129(1):151–162.
- 540 Longuet-Higgins, M. S. (1970). Longshore currents generated by obliquely
541 incident sea waves. *Journal of geophysical research*, 75(33):6778–
542 6789.
- 543 Longuet-Higgins, M. S. and Stewart, R. (1964). Radiation stresses in water
544 waves; a physical discussion, with applications. In *Deep sea research
545 and oceanographic abstracts*, volume 11, pages 529–562. Elsevier.
- 546 Madsen, O. S., Poon, Y.-K., and Gruber, H. C. (1989). Spectral wave
547 attenuation by bottom friction: Theory. In *Coastal Engineering 1988*,
548 pages 492–504.
- 549 Malmstadt, J., Scheitlin, K., and Elsner, J. (2009). Florida hurricanes and
550 damage costs. *southeastern geographer*, 49(2):108–131.
- 551 Marsooli, R., Lin, N., Emanuel, K., and Feng, K. (2019). Climate change
552 exacerbates hurricane flood hazards along US Atlantic and Gulf Coasts
553 in spatially varying patterns. *Nature communications*, 10(1):1–9.
- 554 McWilliams, J. C. and Sullivan, P. P. (2000). Vertical mixing by Langmuir
555 circulations. *Spill Science & Technology Bulletin*, 6(3-4):225–237.
- 556 Mei, C. C. (1989). *The applied dynamics of ocean surface waves*, volume 1.
557 World scientific.
- 558 Moon, I.-J., Ginis, I., Hara, T., and Thomas, B. (2007). A physics-based
559 parameterization of air–sea momentum flux at high wind speeds and
560 its impact on hurricane intensity predictions. *Monthly weather review*,
561 135(8):2869–2878.

- 562 Pinelli, J.-P., Roueche, D., Kijewski-Correa, T., Plaz, F., Prevatt, D., Zisis,
563 I., Elawady, A., Haan, F., Pei, S., Gurley, K., et al. (2018). Overview
564 of damage observed in regional construction during the passage of
565 Hurricane Irma over the State of Florida. In *Forensic Engineering 2018: Forging Forensic Frontiers*, pages 1028–1038. American Society of
566 Civil Engineers Reston, VA.
- 567
- 568 Powell, M. D., Houston, S. H., Amat, L. R., and Morisseau-Leroy, N. (1998).
569 The HRD real-time hurricane wind analysis system. *Journal of Wind
570 Engineering and Industrial Aerodynamics*, 77:53–64.
- 571 Powell, M. D., Vickery, P. J., and Reinhold, T. A. (2003). Reduced drag coeffi-
572 cient for high wind speeds in tropical cyclones. *Nature*, 422(6929):279–
573 283.
- 574 Röhrs, J., Christensen, K. H., Hole, L. R., Broström, G., Drivdal, M., and
575 Sundby, S. (2012). Observation-based evaluation of surface wave
576 effects on currents and trajectory forecasts. *Ocean Dynamics*, 62(10–
577 12):1519–1533.
- 578 Schott, F. A., Lee, T. N., and Zantopp, R. (1988). Variability of structure and
579 transport of the Florida Current in the period range of days to seasonal.
580 *Journal of Physical Oceanography*, 18(9):1209–1230.
- 581 Shinn, E. A. (1988). The geology of the Florida Keys. *Oceanus*, 31(1):46–53.
- 582 Siadatmousavi, S. M., Jose, F., and Stone, G. (2011). Evaluation of two WAM
583 white capping parameterizations using parallel unstructured SWAN
584 with application to the Northern Gulf of Mexico, USA. *Applied Ocean
585 Research*, 33(1):23–30.
- 586 Sikirić, M. D., Roland, A., Janečković, I., Tomazić, I., and Kuzmić, M. (2013).
587 Coupling of the Regional Ocean Modeling System (roms) and Wind
588 Wave Model. *Ocean Modelling*, 72:59–73.
- 589 Smith, N. P. (1982). Response of Florida Atlantic shelf waters to hurricane
590 David. *Journal of Geophysical Research: Oceans*, 87(C3):2007–2016.
- 591 Stokes, G. G. (1880). On the theory of oscillatory waves. *Transactions of
592 the Cambridge philosophical society*.

- 593 Tolman, H. L. et al. (2009). User manual and system documentation of
594 WAVEWATCH III TM version 3.14. *Technical note, MMAB Contribution*,
595 276:220.
- 596 Van Den Bremer, T. and Breivik, Ø. (2018). Stokes drift. *Philosophical Trans-*
597 *actions of the Royal Society A: Mathematical, Physical and Engineering*
598 *Sciences*, 376(2111):20170104.
- 599 Villas Bôas, A. B., Cornuelle, B. D., Mazloff, M. R., Gille, S. T., and Arduin,
600 F. (2020). Wave–current interactions at meso-and submesoscales:
601 Insights from idealized numerical simulations. *Journal of Physical*
602 *Oceanography*, 50(12):3483–3500.
- 603 Weisberg, R., Liu, Y., and Mayer, D. (2009). Mean circulation on the west
604 Florida continental shelf observed with long-term moorings. *Geophys.*
605 *Res. Lett*, 36:L19610.
- 606 Weisberg, R. H. and Zheng, L. (2006). Hurricane storm surge simulations
607 for Tampa Bay. *Estuaries and Coasts*, 29(6):899–913.
- 608 Wu, L., Chen, C., Guo, P., Shi, M., Qi, J., and Ge, J. (2011). A FVCOM-
609 based unstructured grid wave, current, sediment transport model, I.
610 Model description and validation. *Journal of Ocean University of China*,
611 10(1):1–8.
- 612 Xian, S., Feng, K., Lin, N., Marsooli, R., Chavas, D., Chen, J., and Hatzikyri-
613 akou, A. (2018). Brief communication: Rapid assessment of damaged
614 residential buildings in the Florida Keys after Hurricane Irma. *Natural*
615 *Hazards and Earth System Sciences*, 18(7):2041–2045.
- 616 Zedler, S., Niiler, P., Stammer, D., Terrill, E., and Morzel, J. (2009). Ocean’s
617 response to Hurricane Frances and its implications for drag coefficient
618 parameterization at high wind speeds. *Journal of Geophysical Re-*
619 *search: Oceans*, 114(C4).
- 620 Zhang, C., Durgan, S. D., and Lagomasino, D. (2019). Modeling risk of man-
621 groves to tropical cyclones: A case study of Hurricane Irma. *Estuarine,*
622 *Coastal and Shelf Science*, 224:108–116.